Configuration and Dynamics of Hydride Ions in the Nitride-Hydride Catalyst Ca$_3$CrN$_3$H

(article starts on next page)

Article

Configuration and Dynamics of Hydride Ions in the Nitride-Hydride Catalyst Ca$_3$CrN$_3$H

Lucas Fine, Rasmus Lavén, Zefeng Wei, Tatsuya Tsumori, Hiroshi Kageyama, Ryoichi Kajimoto, Mónica Jimenéz-Ruiz, Michael Marek Koza, and Maths Karlsson*

Read Online

ACCESS | 📊 Metrics & More | 📖 Article Recommendations | 🆂�🅸 Supporting Information

ABSTRACT: We report results on the configuration and vibrational dynamics of hydride ions (H⁻) in the novel mixed-anion, nitride-hydride, catalyst Ca$_3$CrN$_3$H by means of variable temperature inelastic neutron scattering experiments, harmonic phonon calculations, and machine-learning molecular dynamics calculations. The combined analyses of experimental and theoretical data show that the vibrational dynamics of H⁻ are manifested as a broad, asymmetric vibrational band between 80 and 130 meV. These vibrational dynamics are generally anharmonic in nature and polarized along the crystallographic c axis, and their dispersive character reveals significant interactions between neighboring H⁻ in the material. We find that most H⁻ are surrounded by two other H⁻ and that the H⁻ sites of the studied sample have an occupancy of at least 95%. We argue that this high H⁻ occupancy may be related to the material's high efficiency as a catalyst for ammonia synthesis.
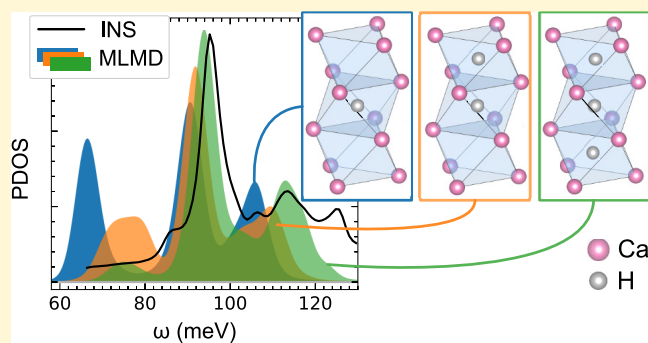
1. INTRODUCTION

Mixed-anion materials, that is, solid-state materials containing more than one anionic species in the same phase, e.g., oxide-hydrides and nitride-hydrides, can exhibit unique properties that are unattainable with their single-anion counterparts.[1,2] Such properties include photocatalytic activity,[3,4] ferroelectricity,[5] superconductivity,[6,7] and photoluminescence,[8] to name a few. Much research in this field has been focused on materials with the antiperovskite structure, i.e., X$_3$BA, where X is a cation and A and B are anions, due to their functionality as ionic conductors and/or as catalysts.[9−11] Of specific concern in this study is the antiperovskite hexagonal phase of the nitride-hydride Ca$_3$CrN$_3$H. This material is obtained by a novel topochemical reaction of the orthorhombic structured Ca$_3$CrN$_3$.[12] Importantly, it shows promise as a catalyst for ammonia synthesis,[13] and its efficient catalytic activity is partly attributed to the diffusion of H⁻ within the crystal structure.[13]

Powder X-ray diffraction (PXRD) measurements of Ca$_3$CrN$_3$H have shown[12] that it is an X$_3$BA-type antiperovskite with X = Ca^{2+}, B = H⁻, and A = [CrN$_3$]$^{5-}$, with the Ca^{2+} ions organized in face-sharing HCa$_6$ octahedra stacked along the crystallographic c axis and bridging [CrN$_3$]$^{5-}$ planar moieties (Figure 1). It belongs to the space group $P6_3/m$. Interestingly, this channel-like structure accommodating hydride ions is unique within the antiperovskite class, to the best of our knowledge. However, because of the insensitivity of X-rays to hydrogen species, the PXRD patterns of Ca$_3$CrN$_3$H and its

hydrogen-free hexagonal counterpart Ca$_3$CrN$_3$ barely differ and are hardly distinguishable.[12] Therefore, the actual H⁻ stoichiometry and local coordination environment of the H⁻ anions in Ca$_3$CrN$_3$H were not determined in the previous PXRD study.[12] Indeed, Rietveld refinement of the PXRD data together with thermogravimetric and mass spectrometric analyses indicate that Ca$_3$CrN$_3$H is nonstoichiometric and rather corresponds to the composition Ca$_3$CrN$_3$H$_x$, with x between 0.7 and 1.[12] In particular, the local coordination environment (configuration) of H⁻, which may be inferred from the vibrational dynamics of the material,[14] is unclear.

A powerful technique to investigate the configuration and vibrational dynamics of hydrogen species in solid-state materials is given by inelastic neutron scattering (INS) coupled to density functional theory (DFT) calculations.[14−16] This is because neutrons are very sensitive to hydrogen species, and the frequencies and intensities of INS spectra can be generally computed on an absolute scale.[17] Therefore, the experimentally determined vibrational frequencies of H⁻ in Ca$_3$CrN$_3$H may, when compared to the DFT-determined
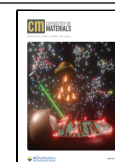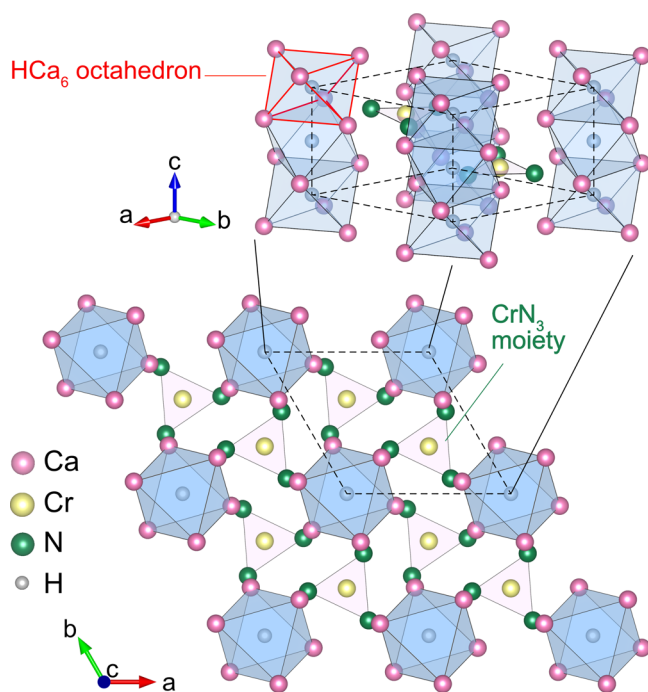
Figure 1. Schematic crystal structure of Ca$_3$CrN$_3$H, adapted with permission from ref 12. Copyright [2024] [John Wiley and Sons]. The dashed lines indicate the unit cell used in the computer calculations (see Section 3). The red lines indicate a HCa$_6$ octahedron.

spectra, serve as a fingerprint of both the configuration and dynamics of the H$^-$ present. Sometimes, machine-learning molecular dynamics (MLMD) calculations can be chosen instead of traditional DFT approaches for the benefit of a reduced computational cost, allowing calculations in larger cells and at several temperatures, and because it can probe the anharmonic behavior of the vibrations.[18,19] Using a combination of INS and MLMD calculations, we here investigate the configuration and vibrational dynamics of H$^-$ in Ca$_3$CrN$_3$H. The results unravel significant interactions between neighboring H$^-$ in a unique, chain-like, structural arrangement of H$^-$, from which we can also determine the actual H$^-$ stoichiometry in the sample.

2. EXPERIMENTAL DETAILS

2.1. Sample Synthesis. Approximately 4 g of Ca$_3$CrN$_3$H powder was prepared following the procedure as reported in ref 12. A starting material of Ca$_3$CrN$_3$ was first treated with H$_2$ gas (>99.99999%) at 450 °C for 2 h and then treated at 400 °C for 24 h (heating and cooling rates of 100 °C/h) with a mixed gas of N$_2$/H$_2$/Ar in the respective proportions of 22.5:67.5:10. The purity and crystal structure of the obtained powder sample was verified by PXRD at the beamline BL02B2 at the SPring-8 synchrotron X-ray facility in Japan.[20] BL02B2 was used with an incident photon wavelength of λ = 0.41947(1) Å and a Debye−Scherrer camera, and the powder sample was contained in a Lindemann glass capillary of 0.3 mm inner diameter. All manipulations of the sample were carried out in a glovebox filled with He gas. The crystal structure was found to belong to the $P6_3/m$ space group with unit-cell parameters a = 7.2280(3) Å and c = 5.0642(2) Å at 300 K.

2.2. INS. The INS measurements were performed on 4SEA-SONS[21,22] at the Japan Proton Accelerator Research Complex and on IN1-Lagrange[23,24] at the Institut Laue Langevin. Approximately 1.3 g of powder sample was evenly distributed inside an aluminum foil that was subsequently rolled into a 14 mm diameter and 44 mm long

cylinder. The sample was inserted into a cylindrical aluminum cell and sealed with a stainless steel metal ring.

The measured INS intensity contains information about vibrational dynamics in Ca$_3$CrN$_3$H and is proportional to the dynamical structure factor $S(Q, \omega)$, where Q and ω are the momentum and energy transfer, respectively. With regard to the measurements on 4SEASONS, we used incident energies of E_i = 299 (16.6 meV), 156 (6.8 meV), 95.2 (3.5 meV), and 64.2 meV (2.1 meV), where the values in parentheses refer to the energy resolutions at zero energy transfer. The frequency of the Fermi chopper was set to 600 Hz, and the analyzed Q and ω ranges were 0.5−22.5 Å^{-1} and 5−260 meV, respectively. The measurements were performed at T = 7 K and lasted for 11 h. The data reduction was done with the Utsusemi software[25] and included normalization to monitor counts and efficiency correction of the detectors. With regard to the measurements on IN1-Lagrange, we used a Cu(220) monochromator and a pyrolytic graphite crystals analyzer, with which we analyzed the ω range of 40−140 meV, with an energy resolution of ~2% of the incident energy. As an indirect-geometry spectrometer, IN1-Lagrange has a well-defined trajectory in (Q,ω) space, in which $\omega \propto Q^2$.[26] $S(Q, \omega)$ was obtained from 2 h long measurements upon heating from 10 to 300 K. The data reduction was done with the software Mantid[27] and included normalization to monitor counts. Mantid was also used for the data analysis of the reduced 4SEASONS and IN1-Lagrange data.

2.2.1. Theoretical Considerations. We note that the total cross section, σ, for Ca, Cr, N, and H is 2.8, 3.5, 12, and 82 barns,[28] respectively, which suggests that the predominant part of the scattering on Ca$_3$CrN$_3$H comes from H$^-$ and N$^-$. Moreover, we note that H$^-$ scatters mainly incoherently (the incoherent cross section of H is 80 barns[28]), whereas N$^-$ scatters mainly coherently (the coherent cross section of N is 11 barns[28]), which implies that the measured INS spectra will contain both incoherent and coherent contributions. However, at relatively large Q (i.e., when $Q \gg 2\pi/d \approx$ 2.5 Å^{-1}, with $d \sim$ 2.5 Å being the nearest-neighbor distance in Ca$_3$CrN$_3$H), the coherent intensity is smoothed out due to the finite Q resolution of the instrument.[29] As a result, for one-phonon scattering events, $S(Q, \omega)$ can be expressed in the incoherent approximation[29] as

$$S_{1ph}(Q, \omega) = \sum_a \frac{\sigma_a}{4\pi} \frac{Q^2}{3m_a} e^{-2W_a} \frac{\text{PDOS}_a(\omega)}{2\omega}(n(\omega) + 1) \quad (1)$$

where a indexes the atoms, m_a is the atomic mass, $2W_a = Q^2 u_a^2$ is the Debye−Waller exponent,[17] u_a^2 is the mean square displacement (msd) of atom a, PDOS$_a(\omega)$ denotes the partial vibrational density of state associated with atom a, and $n(\omega)$ is the phonon population factor. Inverting eq 1, the generalized DOS can be calculated as

$$\text{DOS}(\omega) = \sum_a \frac{\sigma_a}{3m_a} \text{PDOS}_a(\omega)$$

$$= \int dQ S_{1ph}(Q, \omega) e^{2W_a} \frac{2\omega}{Q^2} \frac{4\pi}{n(\omega) + 1} \quad (2)$$

where u_H^2 was obtained by fitting $S(Q)$ profiles (see the Supporting Information), and takes on a value of approximately 0.02 Å^2.

3. COMPUTATIONAL DETAILS

The MLMD calculations were conducted using the package Graphics Processing Units Molecular Dynamics (GPUMD v3.9.5)[30,31] based on a neural network-based machine-learning potential called neuroevolution potential (NEP v4),[31] and they were used to compute vibrational properties of Ca$_3$CrN$_3$H$_x$ with $x \leq 1$. The training procedure of the NEP was conducted following an approach successfully used before on similar systems,[32−34] as described below.

3.1. NEP Training Procedure. First, an ab initio MD (AIMD) calculation was conducted in the NVT ensemble using the Vienna Ab-initio Simulation Package (VASP)[35−37] with a supercell containing 185 atoms, including 17 randomly

distributed H^- and 7 randomly distributed H^- vacancies (V_{H^-}), corresponding to the stoichiometry $Ca_3CrN_3H_{0.71}$, which is close to the H^- content previously estimated (0.7–1).[12] The thermostat was set at a temperature decreasing from 400 to 200 K, and the calculation was run during 8 ps by steps of 2 fs. VASP was set with the projector augmented wave (PAW)[38] method and the Perdew–Burke–Ernzerhof (PBE)[39] exchange-correlation functional. The calculation was conducted at the Γ-point, and a cutoff energy of 500 eV was applied to the plane wave basis. Electronic structures were converged to energies within 10^{-5} eV. In the AIMD trajectory, snapshots were extracted every 100 fs (a total of 72 snapshots), and the energy, forces, and stresses in each snapshot were used to train a NEP (further referred to as the first-generation NEP). The NEP training used radial and angular descriptor cutoffs at 8 and 4 Å, respectively, 30 neurons, and converged within the 1000000 maximal number of generations. Second, the first-generation NEP was used to run MD simulations of 20 ps on 10 supercells including 0–18 randomly distributed V_{H^-}, corresponding to the stoichiometries $Ca_3CrN_3H_x$ with x in the range of 0.25–1, at 100, 200, 400, and 600 K using the NPT ensemble. In each trajectory, snapshots every 100 fs were taken after the temperature and volume stabilization (a total of 400 snapshots). The energy, forces, and stresses in each snapshot were subsequently computed with VASP using the same settings as above, which constituted the second-generation training data set. Finally, a new NEP was trained using the first- and second-generation data sets (a total of 472 snapshots), with the same descriptors, neurons, and maximal number of generations as above. This NEP accurately reproduces the forces and energies calculated with DFT (see Supporting Information for details) and is the one used in further calculations.

3.2. Harmonic Phonons and Dispersion Curves. The vibrational modes and energies were first calculated in the harmonic approximation using the NEP with a finite displacements approach as implemented in the software packages Phonopy[40,41] and Calorine.[31] A supercell of $2 \times 2 \times 2$ unit cells (a unit cell is depicted in Figure 1), containing 128 atoms, was used to model Ca_3CrN_3H, and a similar supercell containing 120 atoms was used to model $Ca_3CrN_3H_{0.5}$. These supercells were relaxed to forces below 10^{-4} eV/Å using the NEP. Then, the force constants were calculated using the NEP and used to compute the phonon eigenvectors and eigenfrequencies. The atom-projected (partial) vibrational density of states (PDOS) was calculated on a q-mesh of $31 \times 31 \times 31$ points and can be expressed as[40]

$$\text{PDOS}_a(\omega, \, \hat{\mathbf{n}}) = \frac{1}{N} \sum_{(\mathbf{q}, \, \nu)} \delta(\omega - \omega_\nu(\mathbf{q})) |\hat{\mathbf{n}} \cdot \mathbf{e}_\nu(a, \, \mathbf{q})|^2 \tag{3}$$

Here, $N = 8$ is the number of unit cells in the calculation, a is the atom index, $\hat{\mathbf{n}}$ is the unit projection direction vector, and $\omega_\nu(\mathbf{q})$ and $\mathbf{e}_\nu(a, \, \mathbf{q})$ are the eigenfrequency and eigenvector of mode $(\mathbf{q}, \, \nu)$. The phonon dispersion curves were calculated along a hexagonal path of 459 q-points within the hexagonal Brillouin zone.

The validity of the harmonic phonon calculations using the NEP was confirmed by repeating the calculation using DFT to compute the force constants (details in the Supporting Information).

The experimental $S(Q, \omega)$ was simulated with the software package OCLIMAX,[42] using the calculated PDOS and the geometry of 4SEASONS. The calculation included multiphonon contributions up to the 10th order.

3.3. MLMD Vibrational Density of State. The NEP was finally used to run MD simulations of $Ca_3CrN_3H_x$ with x in the range of 0.64–1, modeled by large supercells containing 1466–1536 atoms, and at temperatures in the range of 10–300 K. The simulations were first conducted during 200 ps in the NPT ensemble for temperature and volume stabilization and then conducted during 100 ps in the NVE ensemble for the vibrational DOS analysis. Additional calculations were conducted by using the NVT ensemble for temperature and pressure stabilization, followed by a run with the NVE ensemble for analysis. The PDOS was computed from the Fourier transform of the velocity autocorrelation function, as implemented in GPUMD.

Due to the presence of H^- vacancies, 3 inequivalent H^- configurations can be found (considering only nearest neighboring H^- sites) in the supercells, here labeled as $H^- - H^- - H^-$, $H^- - H^- - V_{H^-}$, and $V_{H^-} - H^- - V_{H^-}$ (see Figure 2). $H^- - H^- - H^-$ corresponds to H^- which are flanked by two

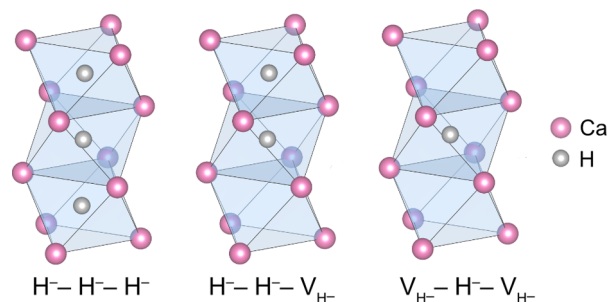**Figure 2.** Schematics of the 3 inequivalent H^- configurations existing in the AIMD calculation.

H^- in first neighbor positions, $H^- - H^- - V_{H^-}$ corresponds to H^- having a unique H^- first neighbor, and $V_{H^-} - H^- - V_{H^-}$ corresponds to H^- which are isolated with no first neighbor H^-.

4. RESULTS AND DISCUSSION

4.1. INS Spectra. Figure 3a shows the $S(Q, \omega)$ map of Ca_3CrN_3H, as measured on 4SEASONS at 7 K for the four different incident energies. Because the intensity below 40 meV contains contributions from the aluminum container, which was not subjected to a separate measurement in our experiment, this part was ignored in our detailed analysis. Above 40 meV, the INS data are characterized by a series of bands; however, for energies higher than 140 meV, the bands are related to second-order transitions, i.e., to scattering events involving two-phonon modes,[17] which will not be analyzed explicitly here. The assignment to second-order transitions is supported both by our computational results and the experimental band energies, which are found to be multiples of the energies of the respective fundamental modes in the interval 90–130 meV (see Supporting Information). For our more detailed analysis, we hence focused on the energy range between 40 and 140 meV. This analysis showed that the INS spectrum can be adequately reproduced by a sum of 8, well-separated Gaussian components ($\omega_1 - \omega_8$), plus a flat background (Figure 3b). For comparison, Figure 3b,c show
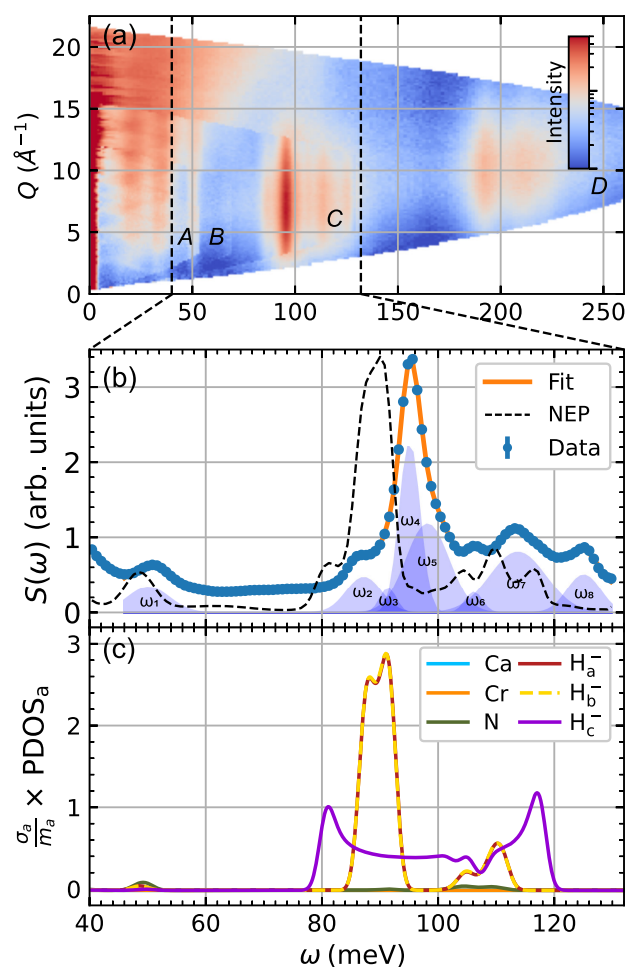
Figure 3. (a) Combined presentation of overlaying $S(Q, \omega)$ maps (A, B, C, D) of Ca_3CrN_3H, as measured on 4SEASONS at 7 K with four incident neutron energies: 64.2 meV (A), 95.2 meV (B), 156 meV (C), and 299 meV (D). In order to be comparable, spectra A, B and C were normalized such that the intensity between 20 and 40 meV is continuous along Q. Spectrum D was normalized such that the maximum intensity at 95 meV matches the maximum intensity of spectrum C at 95 meV. (b) $S(\omega)$ obtained by Q-integration of spectrum C, together with a fit of the peaks with Gaussians (shaded areas) and a theoretical INS spectrum of Ca_3CrN_3H obtained from the phonon calculation and OCLIMAX (dashed line). (c) PDOS of Ca_3CrN_3H from the phonon calculation using the NEP, weighted by the total neutron cross section and the atomic mass of each element. H_a^-, H_b^-, and H_c^- denote the PDOS of H^- projected along the a, b, and c axis, respectively.

the theoretical spectrum, as obtained from the phonon calculation using NEP. As can be observed, the theoretical spectrum shows the same main features and is overall similar to the experimental spectrum, which suggests that the modeled structure provides a good description of the structure of the real material. Therefore, by comparing the experimental and calculated vibrational energies, we can assign the bands to specific vibrational motions. The suggested band assignment is summarized in Table 1. As can be seen from the table, the calculation successfully models the vibrational energies of the Cr−N bending mode (ω_1), with a deviation of less than 3 meV from the experimental data. However, the contributions from hydrogen of the theoretical spectrum are globally downshifted with 3−9 meV compared to the experimental data. This can be attributed to a general overestimation of the equilibrium

Table 1. Experimental Vibrational Energies (in meV) from Fits with Gaussian Components (See Figure 3b), Calculated Frequencies (in meV), and Suggested Band Assignment for Ca_3CrN_3H

band	exp.	calc.	proposed assignment
ω_1	50.7	48.5	Cr−N bending motions
ω_2	86.9	81.2	in-phase H^- motions along c
$\omega_3{}^a$	91.3		
ω_4	94.9	88.2	H^- motions in ab-plane
ω_5	97.8	91.1	H^- motions in ab-plane
ω_6	106	104	H^- motions along a, b, and c
ω_7	113	110	H^- motions along a, b, and c
ω_8	125	116	out-of-phase H^- motions along c

$^a\omega_3$ accounts for the asymmetry of the surrounding ω_2 and ω_4 peaks and was not calculated.

volume by the PBE functional, as it was already observed in $BaTiO_3$ and the oxide-hydride $BaTiO_{2.75}H_{0.125}$.[14,43]

4.2. Hydrogen Local Coordination Environment. We observe that the in-phase and out-of-phase vibrations (ω_2 and ω_8, respectively) of H along the c axis (H_c^-) are located at different energies, indicating that the H_c^- vibrations are dispersive, which is confirmed by the phonon dispersion curve of Ca_3CrN_3H, as shown in Figure 4a. Such a dispersive
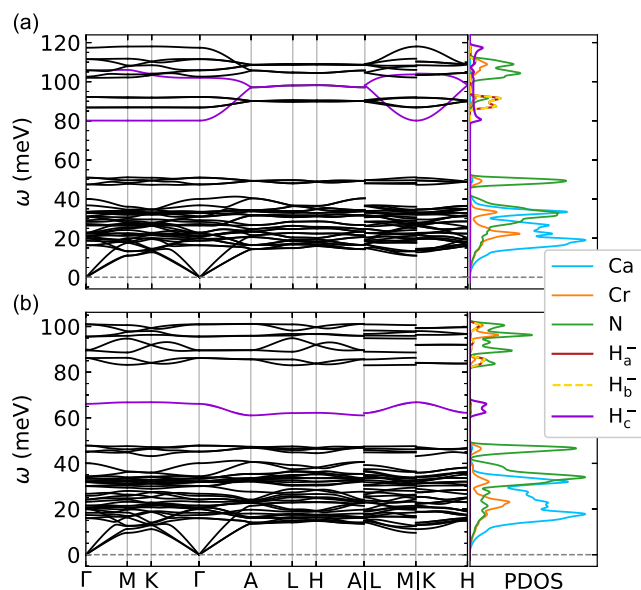

Figure 4. Dispersion curve and PDOS of (a) Ca_3CrN_3H and (b) $Ca_3CrN_3H_{0.5}$, as obtained from the NEP in harmonic calculations. The purple line in the dispersion curves highlights the dispersive and nondispersive character of the H_c^- vibrations in Ca_3CrN_3H and $Ca_3CrN_3H_{0.5}$, respectively.

character reflects a significant interaction between neighboring H^- anions, due to their relative close proximity (2.5 Å along the c axis). Conversely, no dispersion is expected in $Ca_3CrN_3H_{0.5}$ (see Figure 4b), as the lack of H^- in every other H^- site extends their mutual distance up to 5 Å along the c axis, thereby reducing their interaction. As a result, in $Ca_3CrN_3H_{0.5}$, the PDOS of H_c^- has a higher intensity and a lower vibrational energy than in Ca_3CrN_3H. These observations imply that the vibrational dynamics of H^- are correlated to the occupation of their surrounding H^- sites, and, as a

result, that the average H^- occupation in Ca_3CrN_3H can be probed *via* its INS spectrum.

We turn now to the MLMD calculations of the compositions $Ca_3CrN_3H_x$ with x in the range of 0.64−1. Figure 5 shows the

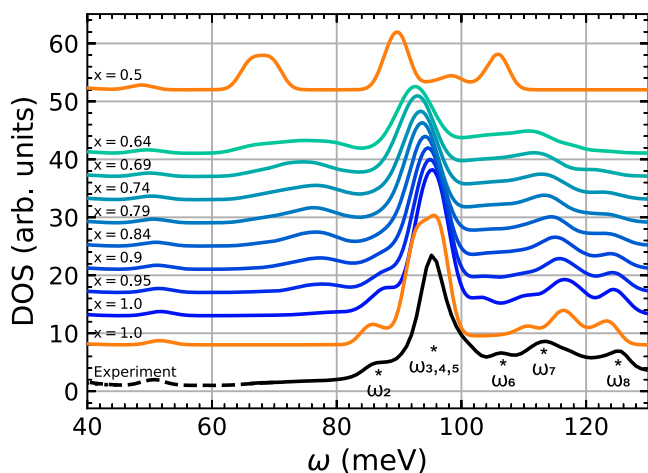**Figure 5.** Comparison of the experimental and computed DOS: (blue lines) DOS for $Ca_3CrN_3H_x$ with x in the 0.64−1 range extracted from the MLMD trajectories at 100 K, weighted by the total neutron cross section and atomic masses. (orange lines) DOS for Ca_3CrN_3H and $Ca_3CrN_3H_{0.5}$ from the phonon calculation, weighted by the total neutron cross section and the atomic masses. (black lines) experimental DOS extracted from the INS data using eq 2 with (continuous black line) the data recorded at E_i = 156 meV and (dashed black line) the data recorded at E_i = 95.2 meV. The computed DOS lines are shifted vertically for clarity and scaled horizontally by a factor of 1.055 in order to match the experimental data.

computed DOS for the various H^- contents, together with the experimental DOS. A main observation is the excellent agreement between the computed and experimental DOS for x = 1. With decreasing x, we observe a gradual decrease in the intensity of the high-energy peak ω_8, as related to out-of-phase vibrations, and a down-shift and broadening in the energy of the peak ω_2, related to in-phase vibrations, already at x = 0.95. In the experiment, no such down-shift is observed, and the peak ω_8 is well visible, which indicates that for our sample x > 0.95. We note that this high H^- content may be at the origin of the efficient ammonia synthesis activity of $Ca_3CrN_3H_x$, as the surface H^- is suspected to participate in the hydrogenation of the N_2 molecules.[13]

The down-shift of the ω_2 peak and the decrease in intensity of the ω_8 peak with decreasing x can be understood by separating the contributions of each H^- configuration in the PDOS, as shown in Figure 6 for x = 0.64. The PDOS for the 3 configurations are overall quite similar but show some marked differences. In particular, we observe that the ω_8 peak is only present for the configuration $H^-−H^-−H^-$, whereas the ω_2 peak down-shifts in energy and increases in intensity for $V_{H^-}−H^-−V_{H^-}$. As a result, it is the transformation of configurations of the type $H^-−H^-−H^-$ into configurations of the type $H^-−H^-−V_{H^-}$ and $V_{H^-}−H^-−V_{H^-}$ with decreasing x which induces a decrease in intensity of the ω_8 peak and a down-shift and broadening of the ω_2 peak. Another observation is a weak down-shift of the peaks ω_3, ω_4, and ω_5 (referred to as the ensemble $\omega_{3,4,5}$) with decreasing x. $\omega_{3,4,5}$ is related to vibrations in the *ab*-plane, and the observed down-shift is due to an
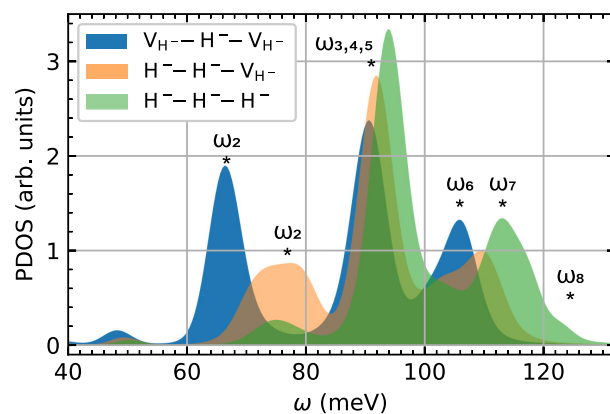
Figure 6. PDOS from each H^- configuration in $Ca_3CrN_3H_{0.64}$ extracted from the MLMD trajectory at 100 K. The supercell includes 43 configurations of the type $H^-−H^-−H^-$, 62 configurations of the type $H^- − H^- − V_{H^-}$, and 17 configurations of the type $V_{H^-} − H^- − V_{H^-}$. The lines are scaled horizontally by a factor of 1.055 in order to match the experimental data.

increase of the lattice constants a and b with decreasing x (see Supporting Information for details).

4.3. Temperature Dependence. Next, we turn to investigate how the H^- vibrational dynamics are affected by temperature. Figure 7 shows variable temperature (10−300 K) INS spectra, as measured on IN1-Lagrange, together with the

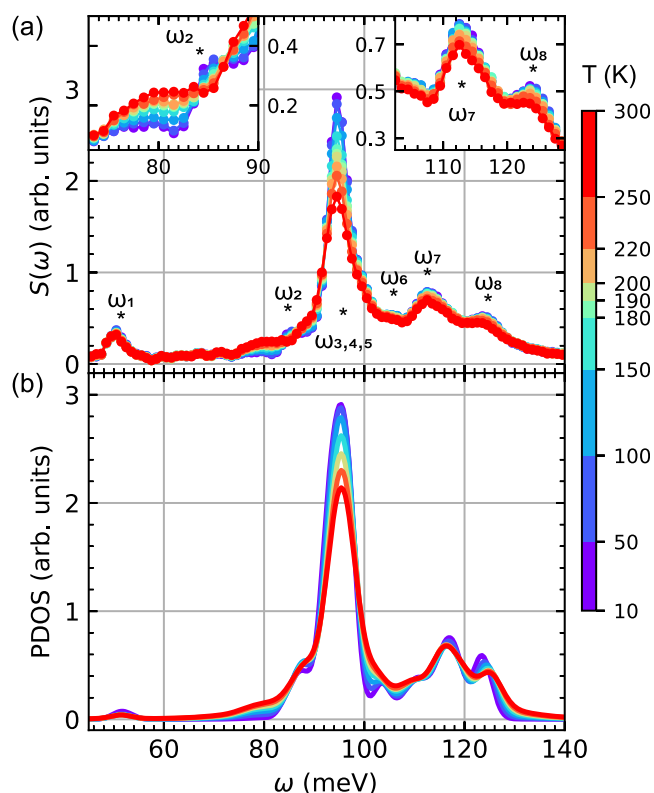**Figure 7.** (a) $S(\omega)$ of Ca_3CrN_3H as measured on IN1-Lagrange at various temperatures. Insets show close-up views for the regions around 80 and 120 meV, respectively. (b) Computed PDOS of H^- for Ca_3CrN_3H as extracted from the MLMD trajectories stabilized in the NPT ensemble at the same temperatures. The PDOS lines are scaled horizontally by a factor of 1.055 in order to match the experimental data.

computed PDOS of H^- for Ca_3CrN_3H, in the same temperature range. In the experiment, the most pronounced effects of increasing the temperature are a gradual decrease in intensity by approximately 30% of the ensemble of peaks $\omega_{3,4,5}$, a broadening of the ω_2 peak, and a broad increase in intensity around 80 meV. The gradual decrease in intensity can be partially attributed to the Debye–Waller factor, as the msd of H^- increases with increasing temperature. However, the comparison with the MLMD calculations shows that most of it is to be attributed to a decrease in intensity and a broadening of the ensemble of peaks $\omega_{3,4,5}$ in the PDOS of H^-. Similarly, the broadening of the ω_2 peak and the increase in intensity around 80 meV is well reproduced in the MLMD calculations, which indicates that these features originate from a change in the PDOS of H^-.

Overall, the temperature-dependent features observed experimentally can be attributed to a global broadening of PDOS with increasing temperature. Such a broadening is due to phonon–phonon interactions resulting in an anharmonic behavior of the related modes.[44] Specifically, an analysis of the NEP shows that one of the modes associated with the ensemble of peaks $\omega_{3,4,5}$ deviates significantly from a harmonic behavior (see Supporting Information for details). Moreover, it is found that the ensemble of peaks $\omega_{3,4,5}$ and the peak ω_2 are upshifted in the PDOS when the MLMD calculation is conducted in the NVT ensemble, that is, without volume stabilization, which also indicates anharmonicity. In the NPT ensemble, as the calculation is conducted here, the upshift due to anharmonicity is compensated by a global down-shift due to thermal expansion (see Supporting Information for details). Anharmonic H^- vibrations in Ca_3CrN_3H could suggest additional motions of H^-, such as rattling motions within the HCa_6 octahedra,[44,45] or may be due to the interaction of the s electron pairs of H^- anions with the nearby p electrons of Ca^{2+} cations, known as the lone pair electron mechanism.[44] Interestingly, we note that Ca_3CrN_3H is electrically conducting,[12] and anharmonicity generally leads to a reduction of the thermal conductivity,[46] which suggests that this material may have good thermoelectric properties.

Furthermore, we note that the ω_8 peak does not show a significant temperature dependence in the experiment, while it broadens and up-shifts in the calculated PDOS. This apparent mismatch may indicate that the anharmonic features of the out-of-phase H^- vibrations are not captured in detail by the calculation. The weak temperature dependence of the peaks ω_6 and ω_7 observed in the experiment and in the PDOS may be due to a significant coupling between the H^- motions probed here and the N^{3-} vibrations, which are weakly temperature dependent. In fact, the msd of N^{3-} is weakly temperature dependent in the range of 10–300 K due to stiff Cr–N bonds (according to the DFT calculations, the Cr–N bonds are approximately 50 times stronger than the Ca–H bonds), and the coupling of H^- vibrations with this mode is indicated by a strong participation ratio of N at the frequencies ω_6 and ω_7 (see Supporting Information for details).

5. CONCLUSIONS

To conclude, our combined INS and MLMD simulation study of the technologically relevant novel nitride-hydride Ca_3CrN_3H has unravelled the vibrational character of H^-, as well as the local configuration of H^- in this material's unique, chain-like structural arrangement of H^-. In particular, the results reveal a generally anharmonic dynamics of H^- with

significant interactions between neighboring H^- in the material, and it is found that most H^- are surrounded by two another H^- and that the H^- sites have an occupancy of at least 95%. This high H^- occupancy may be related to the material's high efficiency as a catalyst for ammonia synthesis. In effect, our results indicate that the vibrational properties of Ca_3CrN_3H may be used as indicators for catalytic activity. Such an approach may as well be applicable to other mixed-anion materials, such as $Ca_2N: e^-$, a two-dimensional electride turning into the nitride-hydride Ca_2NH during catalytic activity,[47] or the oxide-hydride $BaTiO_{2.5}H_{0.5}$ in which the lattice hydride also plays a crucial role in the catalytic activity.[48]

■ ASSOCIATED CONTENT

ⓢ Supporting Information

The Supporting Information is available free of charge at https://pubs.acs.org/doi/10.1021/acs.chemmater.4c02897.

Additional INS data and additional calculation data (PDF)

■ AUTHOR INFORMATION

Corresponding Author

Maths Karlsson – *Department of Chemistry and Chemical Engineering, Chalmers University of Technology, Göteborg 412 96, Sweden;* ⓞ orcid.org/0000-0002-2914-6332; Email: maths.karlsson@chalmers.se

Authors

Lucas Fine – *Department of Chemistry and Chemical Engineering, Chalmers University of Technology, Göteborg 412 96, Sweden; Institut Laue Langevin, Grenoble 38042, France*

Rasmus Lavén – *Department of Chemistry and Chemical Engineering, Chalmers University of Technology, Göteborg 412 96, Sweden;* ⓞ orcid.org/0000-0001-8165-461X

Zefeng Wei – *Department of Energy and Hydrocarbon Chemistry, Kyoto University, Kyoto 615-8510, Japan;* ⓞ orcid.org/0000-0001-7508-4294

Tatsuya Tsumori – *Department of Energy and Hydrocarbon Chemistry, Kyoto University, Kyoto 615-8510, Japan;* ⓞ orcid.org/0009-0005-3345-5655

Hiroshi Kageyama – *Department of Energy and Hydrocarbon Chemistry, Kyoto University, Kyoto 615-8510, Japan;* ⓞ orcid.org/0000-0002-3911-9864

Ryoichi Kajimoto – *Materials and Life Science Division, J-PARC Center, Japan Atomic Energy Agency, Tokai 319-1195, Japan*

Mónica Jimenéz-Ruiz – *Institut Laue Langevin, Grenoble 38042, France;* ⓞ orcid.org/0000-0002-9856-807X

Michael Marek Koza – *Institut Laue Langevin, Grenoble 38042, France*

Complete contact information is available at:
https://pubs.acs.org/10.1021/acs.chemmater.4c02897

Notes

The authors declare no competing financial interest.

■ ACKNOWLEDGMENTS

■ REFERENCES

(1) Kageyama, H.; Hayashi, K.; Maeda, K.; Attfield, J. P.; Hiroi, Z.; Rondinelli, J. M.; Poeppelmeier, K. R. Expanding frontiers in materials chemistry and physics with multiple anions. *Nat. Commun.* **2018**, *9*, 772.

(2) Kobayashi, Y.; Tsujimoto, Y.; Kageyama, H. Property Engineering in Perovskites via Modification of Anion Chemistry. *Annu. Rev. Mater. Res.* **2018**, *48*, 303−326.

(3) Maeda, K.; Lu, D.; Domen, K. Direct Water Splitting into Hydrogen and Oxygen under Visible Light by using Modified TaON Photocatalysts with d⁰ Electronic Configuration. *Chem.—Eur. J.* **2013**, *19*, 4986−4991.

(4) Hitoki, G.; Takata, T.; Kondo, J. N.; Hara, M.; Kobayashi, H.; Domen, K. An oxynitride, TaON, as an efficient water oxidation photocatalyst under visible light irradiation ($\lambda \leq$ 500 nm). *Chem. Commun.* **2002**, 1698−1699.

(5) Oka, D.; Hirose, Y.; Kamisaka, H.; Fukumura, T.; Sasa, K.; Ishii, S.; Matsuzaki, H.; Sato, Y.; Ikuhara, Y.; Hasegawa, T. Possible ferroelectricity in perovskite oxynitride SrTaO₂N epitaxial thin films. *Sci. Rep.* **2014**, *4*, 4987.

(6) Hiroi, Z.; Kobayashi, N.; Takano, M. Probable hole-doped superconductivity without apical oxygens in (Ca,Na)₂CuO₂Cl₂. *Nature* **1994**, *371*, 139−141.

(7) AI-Mamouri, M.; Edwards, P. P.; Greaves, C.; Slaski, M. Synthesis and superconducting properties of the strontium copper oxy-fluoride Sr₂CuO₂F₂₊δ. *Nature* **1994**, *369*, 382−384.

(8) Chen, W.-T.; Sheu, H.-S.; Liu, R.-S.; Attfield, J. P. Cation-Size-Mismatch Tuning of Photoluminescence in Oxynitride Phosphors. *J. Am. Chem. Soc.* **2012**, *134*, 8022−8025.

(9) Gao, S.; Tassel, C.; Fujii, S.; Ubukata, H.; Zhu, T.; Zhang, D.; Broux, T.; Saito, T.; Zhong, C.; Yoruk, E.; Yamamoto, K.; Kuwabara, A.; Uchimoto, Y.; Kageyama, H. Na₃H(ZnH₄) Antiperovskite: A Large Octahedral Distortion with an Off-Centering Hydride Anion Coupled to Molecular Hydride. *Chem. Mater.* **2022**, *34*, 6815−6823.

(10) Gao, S.; Broux, T.; Fujii, S.; Tassel, C.; Yamamoto, K.; Xiao, Y.; Oikawa, I.; Takamura, H.; Ubukata, H.; Watanabe, Y.; Fujii, K.; Yashima, M.; Kuwabara, A.; Uchimoto, Y.; Kageyama, H. Hydride-Based Antiperovskites with Soft Anionic Sublattices as Fast Alkali Ionic Conductors. *Nat. Commun.* **2021**, *12*, 201.

(11) Jia, X.; Zhao, Y.; Chen, G.; Shang, L.; Shi, R.; Kang, X.; Waterhouse, G. I. N.; Wu, L.-Z.; Tung, C.-H.; Zhang, T. Ni₃FeN Nanoparticles Derived from Ultrathin NiFe-Layered Double Hydroxide Nanosheets: An Efficient Overall Water Splitting Electrocatalyst. *Adv. Energy Mater.* **2016**, *6*, No. 1502585.

(12) Cao, Y.; Kirsanova, M. A.; Ochi, M.; Al Maksoud, W.; Zhu, T.; Rai, R.; Gao, S.; Tsumori, T.; Kobayashi, S.; Kawaguchi, S.; et al. Topochemical synthesis of Ca₃CrN₃H involving a rotational structural transformation for catalytic ammonia synthesis. *Angew. Chem., Int. Ed.* **2022**, *61*, No. e202209187.

(13) Cao, Y.; Toshcheva, E.; Almaksoud, W.; Ahmad, R.; Tsumori, T.; Rai, R.; Tang, Y.; Cavallo, L.; Kageyama, H.; Kobayashi, Y. Ammonia Synthesis via an Associative Mechanism on Alkaline Earth Metal Sites of Ca₃CrN₃H. *ChemSusChem* **2023**, *16*, No. e202300234.

(14) Eklöf-Österberg, C.; Mazzei, L.; Granhed, E. J.; Wahnström, G.; Nedumkandathil, R.; Häussermann, U.; Jaworski, A.; Pell, A. J.; Parker, S. F.; Jalarvo, N. H.; Börjesson, L.; Karlsson, M. The role of oxygen vacancies on the vibrational motions of hydride ions in the oxyhydride of barium titanate. *J. Mater. Chem. A* **2020**, *8*, 6360−6371.

(15) Ueda, T.; Hayashi, S.; Nakai, Y.; Ikeda, S. Local structure in β−Ti₁₋yVyHx studied by inelastic neutron scattering. *Phys. Rev. B* **1995**, *51*, 5725−5731.

(16) Mazzei, L.; Perrichon, A.; Mancini, A.; Wahnström, G.; Malavasi, L.; Parker, S. F.; Börjesson, L.; Karlsson, M. Local structure and vibrational dynamics in indium-doped barium zirconate. *J. Mater. Chem. A* **2019**, *7*, 7360−7372.

(17) Mitchell, P. C. H.; Parker, S. F.; Ramirez-Cuesta, A. J.; Tomkinson, J. *Vibrational Spectroscopy with Neutrons: With Applications in Chemistry, Biology, Materials Science and Catalysis*; Series on Neutron Techniques and Applications; World Scientific, 2005; Vol. 3.

(18) Gupta, M. K.; Kumar, S.; Mittal, R.; Mishra, S. K.; Rols, S.; Delaire, O.; Thamizhavel, A.; Sastry, P. U.; Chaplot, S. L. Distinct Anharmonic Characteristics of Phonon-Driven Lattice Thermal Conductivity and Thermal Expansion in Bulk MoSe2 and WSe2. *J. Mater. Chem. A* **2023**, *11*, 21864−21873.

(19) Gupta, M. K.; Ding, J.; Bansal, D.; Abernathy, D. L.; Ehlers, G.; Osti, N. C.; Zeier, W. G.; Delaire, O. Strongly Anharmonic Phonons and Their Role in Superionic Diffusion and Ultralow Thermal Conductivity of Cu₇PSe₆. *Adv. Energy Mater.* **2022**, *12*, No. 2200596.

(20) Kawaguchi, S.; Takemoto, M.; Osaka, K.; Nishibori, E.; Moriyoshi, C.; Kubota, Y.; Kuroiwa, Y.; Sugimoto, K. High-throughput powder diffraction measurement system consisting of multiple MYTHEN detectors at beamline BL02B2 of SPring-8. *Rev. Sci. Instrum.* **2017**, *88*, No. 085111.

(21) Kajimoto, R.; et al. The Fermi Chopper Spectrometer 4SEASONS at J-PARC. *J. Phys. Soc. Jpn.* **2011**, *80*, SB025.

(22) Nakamura, M.; Kajimoto, R.; Inamura, Y.; Mizuno, F.; Fujita, M.; Yokoo, T.; Arai, M. First Demonstration of Novel Method for Inelastic Neutron Scattering Measurement Utilizing Multiple Incident Energies. *J. Phys. Soc. Jpn.* **2009**, *78*, No. 093002.

(23) Ivanov, A.; Jimenéz-Ruiz, M.; Kulda, J. IN1-LAGRANGE−the new ILL instrument to explore vibration dynamics of complex materials. *J. Phys. Conf. Ser.* **2014**, *554*, No. 012001.

(24) Lucas, F.; Monica, J. R. *Hydride-Ion Dynamics in the Nitride-Hydride Ca₃CrN₃H*; Institut Laue-Langevin (ILL), 2023.

(25) Inamura, Y.; Nakatani, T.; Suzuki, J.; Otomo, T. Development Status of Software "Utsusemi" for Chopper Spectrometers at MLF, J-PARC. *J. Phys. Soc. Jpn.* **2013**, *82*, SA031.

(26) Parker, S. F.; Ramirez-Cuesta, A. J.; Daemen, L. Vibrational spectroscopy with neutrons: Recent developments. *Spectrochim. Acta. A. Mol. Biomol. Spectrosc.* **2018**, *190*, 518−523.

(27) Arnold, O.; et al. Mantid—Data analysis and visualization package for neutron scattering and μSR experiments. *Nucl. Instrum. Methods Phys. Res. Sect. Accel. Spectrometers Detect. Assoc. Equip.* **2014**, *764*, 156−166.

(28) Sears, V. F. Neutron scattering lengths and cross sections. *Neutron News* **1992**, *3*, 26−37.

(29) Boothroyd, A. T. *Principles of neutron scattering from condensed matter*; Oxford University Press, 2020.

(30) Fan, Z.; Chen, W.; Vierimaa, V.; Harju, A. Efficient Molecular Dynamics Simulations with Many-Body Potentials on Graphics Processing Units. *Comput. Phys. Commun.* **2017**, *218*, 10−16.

(31) Fan, Z.; et al. GPUMD: A Package for Constructing Accurate Machine-Learned Potentials and Performing Highly Efficient Atomistic Simulations. *J. Chem. Phys.* **2022**, *157*, 114801.

(32) Wang, X.; Yang, J.; Ying, P.; Fan, Z.; Zhang, J.; Sun, H. Dissimilar thermal transport properties in κ−Ga₂O₃ and β−Ga₂O₃ revealed by homogeneous nonequilibrium molecular dynamics simulations using machine-learned potentials. *J. Appl. Phys.* **2024**, *135*, No. 065104.

(33) Zhang, J.; Zhang, H.-C.; Li, W.; Zhang, G. Thermal Conductivity of GeTe Crystals Based on Machine Learning Potentials. *Chinese Phys. B* **2024**, *33*, No. 047402.

(34) Fan, Z.; Zeng, Z.; Zhang, C.; Wang, Y.; Song, K.; Dong, H.; Chen, Y.; Ala-Nissila, T. Neuroevolution Machine Learning Potentials: Combining High Accuracy and Low Cost in Atomistic

Simulations and Application to Heat Transport. *Phys. Rev. B* **2021**, *104*, No. 104309.

(35) Kresse, G.; Hafner, J. Ab initio molecular dynamics for liquid metals. *Phys. Rev. B* **1993**, *47*, 558−561.

(36) Kresse, G.; Furthmüller, J. Efficiency of ab-initio total energy calculations for metals and semiconductors using a plane-wave basis set. *Comput. Mater. Sci.* **1996**, *6*, 15−50.

(37) Kresse, G.; Furthmüller, J. Efficient iterative schemes for ab initio total-energy calculations using a plane-wave basis set. *Phys. Rev. B* **1996**, *54*, 11169−11186.

(38) Kresse, G.; Joubert, D. From ultrasoft pseudopotentials to the projector augmented-wave method. *Phys. Rev. B* **1999**, *59*, 1758−1775.

(39) Perdew, J. P.; Burke, K.; Ernzerhof, M. Generalized Gradient Approximation Made Simple. *Phys. Rev. Lett.* **1996**, *77*, 3865−3868.

(40) Togo, A.; Tanaka, I. First principles phonon calculations in materials science. *Scr. Mater.* **2015**, *108*, 1−5.

(41) Togo, A. First-principles Phonon Calculations with Phonopy and Phono3py. *J. Phys. Soc. Jpn.* **2023**, *92*, No. 012001.

(42) Cheng, Y. Q.; Daemen, L. L.; Kolesnikov, A. I.; Ramirez-Cuesta, A. J. Simulation of Inelastic Neutron Scattering Spectra Using OCLIMAX. *J. Chem. Theory Comput.* **2019**, *15*, 1974−1982.

(43) Wahl, R.; Vogtenhuber, D.; Kresse, G. $SrTiO_3$ and $BaTiO_3$ revisited using the projector augmented wave method: Performance of hybrid and semilocal functionals. *Phys. Rev. B* **2008**, *78*, No. 104116.

(44) Wei, B.; Sun, Q.; Li, C.; Hong, J. Phonon anharmonicity: a pertinent review of recent progress and perspective. *Sci. China Phys. Mech. Astron.* **2021**, *64*, 117001.

(45) Takabatake, T.; Suekuni, K.; Nakayama, T.; Kaneshita, E. Phonon-Glass Electron-Crystal Thermoelectric Clathrates: Experiments and Theory. *Rev. Mod. Phys.* **2014**, *86*, 669−716.

(46) Chang, C.; Zhao, L.-D. Anharmoncity and Low Thermal Conductivity in Thermoelectrics. *Materials Today Physics* **2018**, *4*, 50−57.

(47) Kitano, M.; Inoue, Y.; Ishikawa, H.; Yamagata, K.; Nakao, T.; Tada, T.; Matsuishi, S.; Yokoyama, T.; Hara, M.; Hosono, H. Essential Role of Hydride Ion in Ruthenium-Based Ammonia Synthesis Catalysts. *Chem. Sci.* **2016**, *7*, 4036−4043.

(48) Kobayashi, Y.; Tang, Y.; Kageyama, T.; Yamashita, H.; Masuda, N.; Hosokawa, S.; Kageyama, H. Titanium-Based Hydrides as Heterogeneous Catalysts for Ammonia Synthesis. *J. Am. Chem. Soc.* **2017**, *139*, 18240−18246.